MOVING TOWARDS STABLE METAL HALIDE PEROVSKITE SOLAR CELLS FOR USE IN LOW-EARTH ORBIT

A Dissertation
Presented to
The Academic Faculty

by

Matthew S. Rager

In Partial Fulfillment
of the Requirements for the Degree
Master of Science in the
College of Materials Science and Engineering

Georgia Institute of Technology
December 2019

MOVING TOWARDS STABLE METAL HALIDE PEROVSKITE SOLAR CELLS FOR USE IN LOW-EARTH ORBIT

Approved by:

Dr. Zhiqun Lin, Advisor
School of Materials Science and Engineering
Georgia Institute of Technology

Dr. Zhitao Kang
Georgia Tech Research Institute
Georgia Institute of Technology

Dr. Dong Qin
School of Materials Science and Engineering
Georgia Institute of Technology

Date Approved: [August 15, 2019]

ACKNOWLEDGEMENTS

I would first like to acknowledge my advisor, Dr. Zhiqun Lin, for providing me with guidance throughout my time as a graduate student at Georgia Tech and for giving me the opportunity and resources to explore the field of perovskite solar cells. Thank you also to my co-advisor Dr. Zhitao Kang for providing guidance in my research, helping to fund my stay at Georgia Tech, and for giving his time to be on my defense committee. I also want to thank Dr. Dong Qin for sacrificing her time to be a part of my defense committee. I greatly appreciate it. Thanks to Dr. Jud Ready for allowing me the opportunity to be a part of the project to send solar cells to the International Space State on the MISSE mission. The project was a great challenge, and I am very thankful for the opportunity. I would also like to thank all of my group/lab-mates and collaborators in the Lin lab and beyond. I owe many of you a great debt of gratitude for the help you have given me in, and out, of the lab.

Last, but definitely not least of all, thank you dearly to my family and to my friends for being so patient, understanding, and supportive during my studies. Thank you for the support during the stressful times, the late nights, and weekends in the lab. I could not have made it to this point without you all!

TABLE OF CONTENTS

LIST OF TABLES

LIST OF FIGURES

LIST OF SYMBOLS AND ABBREVIATIONS

MA	Methylammonium
JV	Current-voltage
PSC	Perovskite solar cell
PCE	Power conversion efficiency
LEO	Low-Earth orbit
ETL	Electron transport layer
HTL	Hole transport layer
V_{OC}	Open-circuit voltage
J_{SC}	Short-circuit current
FF	Fill-factor
VBM	Valence band maximum
CBM	Conduction band minimum
t	Goldschmidt tolerance factor
R_{series}	Series resistance
R_{shunt}	Shunt resistance
V_{MP}	Voltage at max power point
J_{MP}	Current at max power point
UV-vis	Ultraviolet-visible absorption spectroscopy
PL	Photoluminescence
IS	Impedance spectroscopy
DMF	N,N-dimethylformamide
DMSO	N,N-dimethylsulfoxide

FTO	Fluorine-doped tin oxide
ISS	International space station
MISSE	Materials international space station experiment
AI	All-inorganic
OI	Organic-inorganic

SUMMARY

Perovskite solar cells have recently emerged as a new leader in the third-generation of photovoltaics. Additionally, this new technology has the potential for application in several areas, including aerospace. The light-absorbing material in perovskite solar cells is an organometal halide compound with the perovskite structure (ABX_3) where various atoms can be combined and interchanged to tune the optoelectronic properties. Typically, the A site is filled by organic, small- molecule cations (e.g. methylammonium and formamdinium) and/or inorganic atoms (e.g. Cs or Rb), the B site is filled by metal atoms (e.g. Pb^{2+} or Sn^{2+}), and halide anions (e.g. I^- and Br^+) fill the X site. In this study, I fabricated organic-inorganic ($MAPbI_3$ and $Cs_{0.05}(MA_{0.17}FA_{0.83})Pb(I_{0.83}Br_{0.17})_3$ and all-inorganic ($CsPbBr_3$) perovskite solar cells to improve the efficiency and stability with the goal of creating devices to operate in the low-Earth orbit environment. The harsh environment of space requires materials with good thermal stability due to large variations in temperature. The organic-inorganic solar cells are more efficient than all-inorganic, but the organic cation places limitations on the thermal stability of the material. Thus, all-inorganic perovskite solar cells (e.g. $CsPbBr_3$) were fabricated and studied as the best candidates to survive the extreme conditions in low-Earth orbit.

CHAPTER 1. INTRODUCTION

Finding a source of sustainable/renewable energy is a high national security priority. While silicon solar cells are now widely used, they are expensive and are limited in their efficiency. Perovskite solar cells (PSCs) have emerged as the next leader of high efficiency, low-cost third-generation photovoltaics. The material methylammonium lead iodide ($CH_3NH_3PbI_3$/$MAPbI_3$) was first used as the photon-absorbing dye in a dye-sensitized solar cell resulting in an efficiency of 3.8% in 2009. [1] This was improved to 10.9% [2] in 2012 by Snaith and co-workers by switching from a dye-sensitized structure to an all-solid state bulk heterojunction structure, which is now the conventional structure, and now PSCs have reached efficiencies up to 22.1% [3]. Figure 1 shows the NREL best efficiency chart which depicts landmark studies in all of the various photovoltaic technologies. Perovskite solar cells (orange line) show a meteoric rise in efficiency compared to other alternatives. The crystal structure of perovskite is defined by the form ABX_3; where A = cation (MA^+, FA^+, Cs^+, Rb^+, etc.), B = metal cation (Pb^{2+}, Sn^{2+}, etc.), and X = halide anion (I^-, Br^-, Cl^-, SCN^-, etc.). The most common and well-studied composition of perovskite used for the photon absorbing material is methyl ammonium lead iodide ($MAPbI_3$). The relatively low band gap (~1.5 eV) and low exciton binding energy (<25meV) are just two of the key properties that contribute to its high photoconversion efficiency [4]. This allows low energy photons to be absorbed and for charges to easily disassociate and become collected by an external load. Due to its unique properties, several other compositions of perovskites have been extensively explored over the past several years.

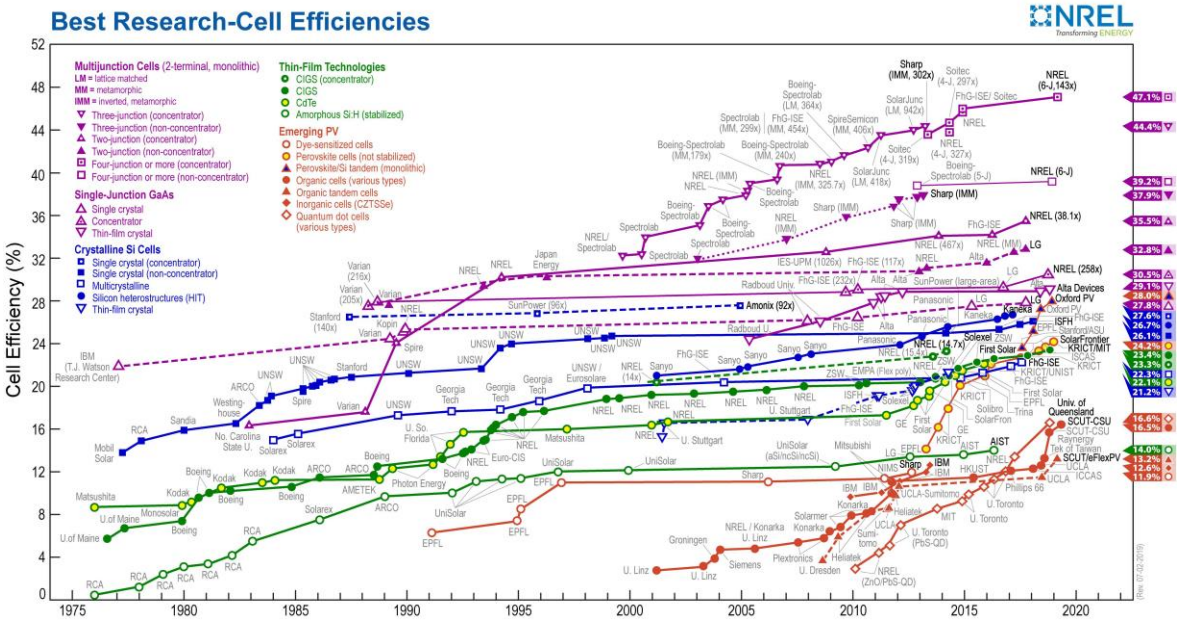

Figure 1 - NREL chart of best photovoltaic efficiencies from 1975 to present.

The applications of PSCs are currently limited due to the instability of the material from moisture, oxygen, light, and heat. Thorough engineering of the light absorbing material and charge extraction layers, along with encapsulation, will likely be necessary to realize lifetimes up to 20 years and beyond. Even with encapsulation, there are issues of ion migration across interfaces and degradation caused by recombination at defects and interfaces in the photovoltaic devices during cycling. Some methods to improve stability involve modification of the perovskite absorber layer itself. H. Tsai and co-workers were able to achieve stability >2000 hrs while cycling under standard 1.5AM illumination by the use of a preferentially oriented 2D Ruddlesden-Popper phase perovskite material.[5] This 2D phase is more stable due to the insulating effects of organic cations intercalated between the perovskite sheets. On the other hand, the charge carrier diffusion is limited to the in-plane direction of the sheets because of the electrically insulating nature of the organic cations. Other work involves design of interfacial barrier layers both organic and

inorganic. Cross-linking of polymer charge transport layers proved to be one way to reduce moisture and oxygen penetration and prevent ion migration [6].

The fast rise of PSC efficiency and the quick pace of research has encouraged exploration into many possible applications. One such area is the aerospace industry. Photovoltaics are used in many instances including the solar array on the International Space Station and solar panels for robotic rovers and spacecraft used power to sensors, telemetry, and other important components. Significant strides have been made in silicon and other inorganic thin-film photovoltaic technologies (e.g. GaAs) for space applications [7]. GaAs is commonly employed because of the higher efficiency compared to Si. This allowed for reduced weight which is key to reducing space flight costs. Multi-junction solar cells are also of high interest since the efficiency can be increased beyond the Shockley-Queisser efficiency limit for a single-junction solar cells [8]. Perovskite materials may offer a low-cost and light-weight alternative because of their tunable bandgap, high power conversion efficiency (PCE) to weight ratio [9], and ability to be used in multi-junction solar cells [10]. Additionally, there are a wide range of compositions from organic-inorganic hybrid perovskite materials to all-inorganic perovskite materials which opens many possible avenues towards developing solar cells with beneficial properties for space applications.

The composition of the perovskite, light-absorbing, layer is the key component to achieving high-efficiency photoconversion. Several studies have explored adding various cations and anions to tune the composition of $MAPbI_3$ to precisely control the properties of the absorber layer. The most common A site additions include Cs^+ and FA^+, but studies have more recently used Rb^+ to stabilize the lattice. By using FA cations instead of MA,

$FAPbI_3$ is formed which has a lower bandgap (~1.45eV) and, due to the larger size of the FA^+ cation, the lead iodide octahedral framework is slightly expanded and forms the cubic phase, in contrast to tetragonal $MAPbI_3$, at room temperature [11]. Mixing these two cations to form a multi-cation perovskite resulted in the suppression of the yellow δ-phase which is unstable and poor light absorbing phase. By adding bromine to the composition, systems such as $FAPb(I_{0.85}Br_{0.15})_3$ were shown to further suppress the formation of the un-wanted δ-phase. This led to the study of mixed-cation and mixed-halide compositions. Controlling the ratio of $FAPbI_3$ to $MAPbBr_3$, to form the composition $(FAPbI_3)_{0.85}(MAPbBr_3)_{0.15}$, led to a noteworthy increase in stability and efficiency of the perovskite α-phase (cubic) [12], and the addition of Cs to the mixed-cation, mixed-halide system, with the composition $Cs_{0.05}(MA_{0.17}FA_{0.83})_{0.95}Pb(I_{0.83}Br_{0.17})_3$ resulted in a landmark efficiency of 21.1% by M. Grätzel and co-workers [13]. Yet, while the mixed-cation, mixed-halide systems are currently the most efficient of the perovskite compositions, they suffer from stability under ambient conditions.

All-inorganic perovskite compositions are one of the growing alternatives to organic-inorganic perovskite solar cells. Research into all-inorganic perovskite solar cells (e.g. $CsPb(Br_xI_{1-x})_3$) has increased because of the superior thermal stability of these materials [14]. That is, these materials can withstand temperatures up to 300°C, which makes them great candidates for use in low-Earth orbit environments which see large variations in temperature up to 120°C and down to -120°C. Although efficiency over 15% was recently reported for $CsPbI_3$ composition, the black, light-absorbing phase is unstable at room temperature and degrades rapidly in ambient conditions without additives to stabilize the lattice [15]. Instead of using additives, which often require adding an organic

component, the halide atom can be tuned to introduce bromine or fabricate $CsPbBr_3$ solar cells. This composition has much better stability to moisture and oxygen, so the solar cells can be processed in ambient atmosphere, and the cubic phase is stable at room temperature [16]. The smaller bromine atom improves the lattice stability, but necessitates a trade off in efficiency due to the increased bandgap [17]. Typically, the PCE of $CsPbBr_3$ solar cells is below 10%, with only a couple recent studies claiming to break the 10% mark [17]. These recent breakthroughs show $CsPbBr_3$ to be a promising alternative for applications in harsh environments.

In this thesis, I will discuss my initial efforts and successes in fabricating perovskite solar cells, with both organic-inorganic and all-inorganic perovskite compositions, with a focus on improving the stability for use in low-Earth orbit (LEO). I began by fabricating the most common organic-inorganic perovskite material $MAPbI_3$ to make efficient solar cells. Additional atoms (Cs^+, FA^+, and Br^-) were added to the $MAPbI_3$ composition to improve the overall efficiency of devices and further improve stability. The conditions of LEO demand a perovskite material that not only has long-term stability under ambient conditions, but also has better temperature stability. Thus, $CsPbBr_3$ solar cells were explored as an alternative candidate following the logic that removing the organic components of the perovskite absorber material will help enable long-term use of perovskite solar cells in aerospace applications. Important considerations and common issues during the fabrication of perovskite solar cells will also be discussed.

CHAPTER 2. WORKING PRINCIPLES OF PEROVSKITE SOLAR CELLS

The mechanism of photoconversion for perovskite solar cells differs from that of commercial silicon and other photovoltaic technologies such as GaAs, CZTS, and organic solar cells. In the case of perovskite materials, there are several distinct advantages that make them efficient at absorbing light and converting to electrical energy.

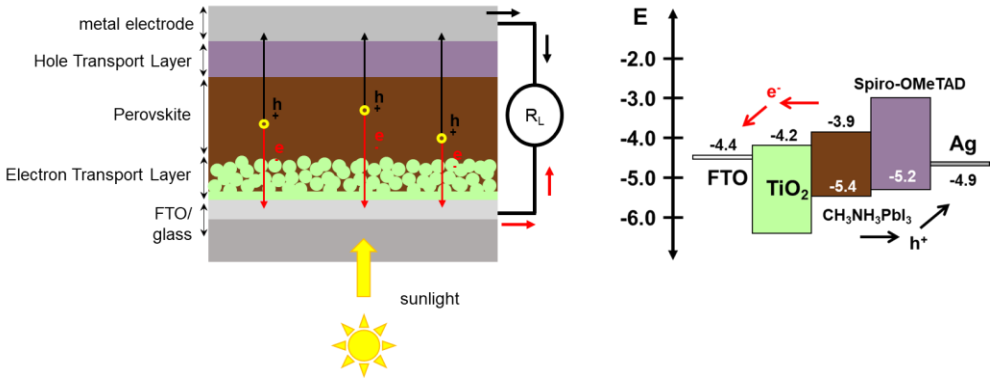

Figure 2 - (left) Schematic of a bulk heterojunction perovskite solar cell under illumination conditions. (right) Energy band diagram corresponding to the bulk heterojunction PSC with TiO_2 as the ETL and Spiro-OMeTAD as the HTL.

Organic-inorganic perovskites have a high absorption coefficient which enables absorption of a large portion of the solar spectrum. Figure 2 shows a general schematic of a bulk heterojunction PSC (left) and the band energy diagram (right) of the stack. The perovskite layer is an intrinsic (ambipolar) semiconductor, which means that electrons and holes are present in approximately the same amount, but may become doped depending on processing procedures. The perovskite material is sandwiched between an n-type (electron transport) layer and a p-type (hole transport) layer, forming an n-i-p junction. When a photon is absorbed by the perovskite material an exciton (electron-hole pair) is formed, as is represented by the yellow dots in fig. 2 – left. At this stage, the electrons and holes are

still loosely bound together, but have not separated into conduction and valence bands. The low exciton binding energy (reported as low as a few meV at room temperature [18]) allows the electrons and holes to easily disassociate from one another since the value is less than the energy at room temperature. The separated charges are transported to respective ETL and HTL due to the small electrical field generated at the interfaces between the perovskite and charge transport materials.

The difference in band edge positions for the respective electron/hole selective contacts provides a small driving force to shuttle charges and transport them into the selective electrodes. Closing the circuit between the bottom electrode (negative in the schematic) and the top electrode of the energy storage device then generates a voltage across a load (e.g. a battery). This, in turn, drives the charging mechanism and allows storing of sunlight harvested energy.

2.1 Perovskite Crystal Structure

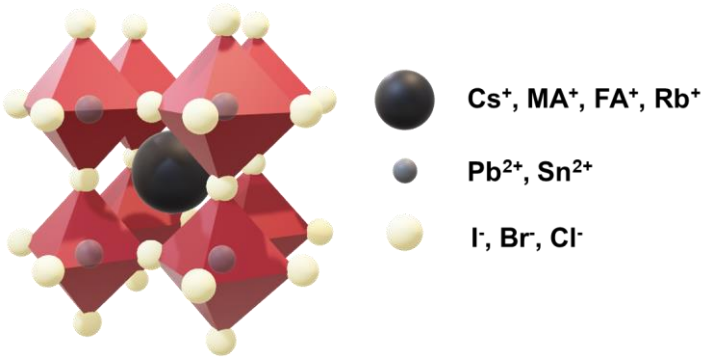

Figure 3 - Crystal structure of ABX_3 perovskite

The crystal structure of the ABX_3 consists of corner-sharing $(BX_6)^{4-}$ octahedrons with the A site filling the interstitial sites of the octahedral framework. Metal cations make up the B site and sit at the center of the octahedral and is surrounded by up to 6 halide

anions The bandgap of the perovskite material has a strong dependence on the $(BX_6)^{4-}$ octahedral framework. In the case of PbI_6, the valence band maximum (VBM) is strongly linked to antibonding of Pb-6s and I-5p orbitals, and the conduction band minimum is determined by the bonding of Pb-6p orbitals [19]. The size and electronic properties of the atoms that make up the crystal structure have an influence on the bandgap and the stability of the crystal structure. The Goldschmidt tolerance factor (*t*) is used to estimate whether or not a given combination of cations and anions can form a stable structure and is defined as $t = (r_A + r_X)/[\sqrt{2}(r_B + r_X)]$ for the perovskite crystal structure. This is based on the effective ionic radii of each atom that makes up the crystal lattice and a stable 3D perovskite structure has a Goldschmidt tolerance factor of t = 0.8-0.9 (note: this is only theoretical and compositions outside this number have been reported). The above equation is targeted towards perovskite oxides, but has been generally applied for the use of organometal halide perovskites [20]. The organometal halide perovskites can exhibit several phases including cubic, tetragonal, trigonal, and orthorhombic. The phase has a large determination on the electronic properties of the material and can be the difference between a functioning and non-functioning solar cell [21]. The cubic (denoted by α) and tetragonal phases form 3D perovskite phases with corner sharing octahedral which allow the material to form a suitable bandgap for light-absorption, whereas, the trigonal and orthorhombic (denoted by δ) phases contain large tilting of octahedral and optoelectronic properties are diminished. Structural phase transitions occur at many different temperature points, depending on the composition, and must be considered when assessing electrical characteristics. For instance, materials that undergo phase transitions during operation may exhibit lower stability due to constant re-arranging of the lattice [22]. Other cubic perovskite

compositions, such as the all-inorganic $CsPbI_3$, are only stable at high temperatures (>300°C) and thus require special processing conditions to stabilize the light-absorbing phase [23]. Thus, compositional engineering has become an effective method controlling the structure-property relationship and improving the overall efficiency and stability of perovskite solar cell devices.

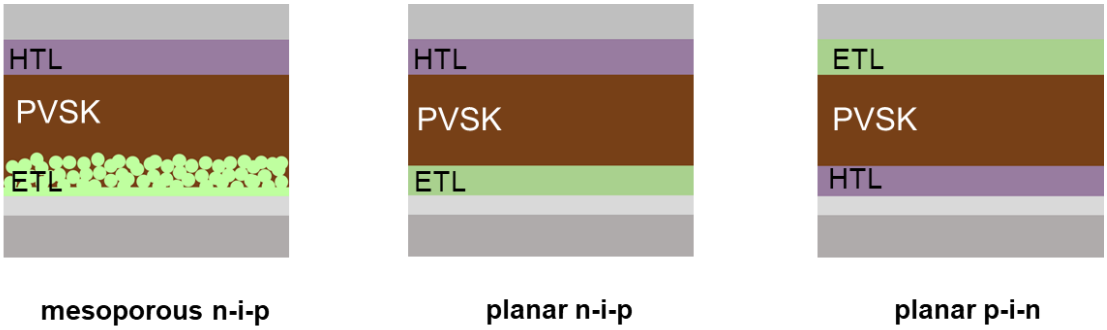

Figure 4 - Conventional architectures of bulk heterojunction perovskite solar cells.

2.2 Charge Transport Materials for Perovskite Solar Cells

The typical perovskite solar cell (PSC) is an all-solid-state device and comprises a bulk heterojunction architecture employing electron (ETL) and hole transporting layers (HTL) which sandwich the perovskite layer to create a p-i-n junction. The transport layers provide a driving force to the disassociated charges in the perovskite layer, and it is critical to tune the properties of these materials such as thickness, charge mobility, and conductivity to balance charge collection rate. This creates interfaces between the absorbing layer and charge transport layers, as well as, transport layers and electrodes. Interfacial defects, polarization at interfaces, and other electronic discontinuities are

sources of charge recombination through formation of trap states which reduce overall device performance. [24] Additionally, poor interfacial contact and morphology also reduces charge transport efficiency.

Typically, the electron transport layers are made of materials ranging from metal-oxide semiconductors, such as TiO_2, to fullerene-based polymers such as PCBM [25]. Many studies have looked at variations of doped metal oxides and different polymers. The hole transport layer is usually made of a polymer material such as Spiro-OMeTAD or PEDOT:PSS, but may also be made of a metal oxide such as NiO, typically in an inverted architecture (HTL on the bottom). Depending on the material properties, band edge positions of the respective transport layers, and contact with the perovskite layer, these interfaces will have expectedly different charge transport characteristics [26]. Engineering the interfacial properties is crucial and a great challenge in developing high-quality perovskite solar cell devices.

2.3 Characterization of Perovskite Solar Cells

The most common, and arguably the most important, technique for photovoltaic characterization is current-voltage (JV) analysis. Typically, JV measurements are used to determine device performance characteristics and provide electrical information such as short-circuit current (J_{SC}), open-circuit voltage (V_{OC}), and series and shunt resistances.

Figure 5 (top) shows a JV curve for a typical solar cell. By plotting the power generated

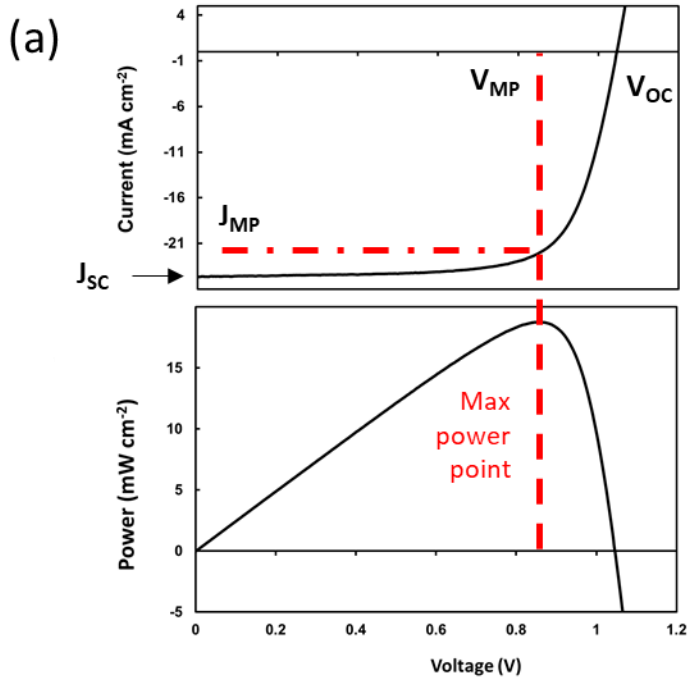

$$FF = \frac{J_{MP} \times V_{MP}}{J_{SC} \times V_{OC}} \qquad PCE = \frac{J_{MP} \times V_{MP}}{P_{sun}}$$

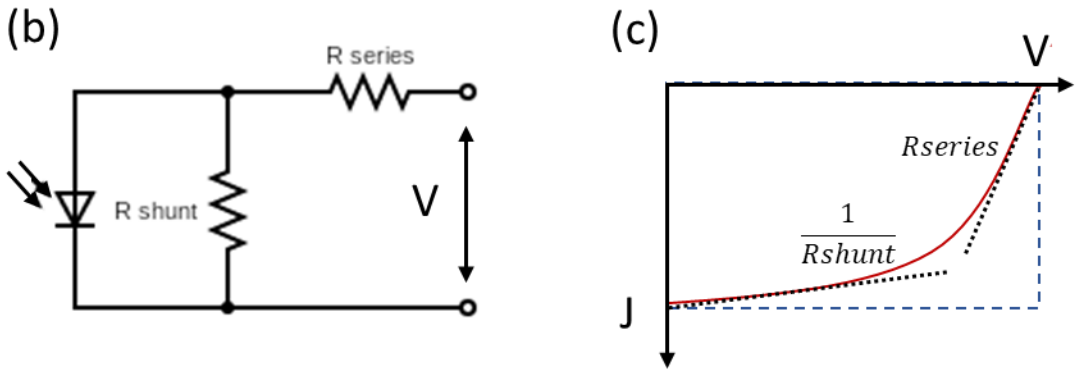

Figure 5 - (a) JV curve and max power point curve for photovoltaic cell under illumination. (b) electrical circuit diagram representing the basic photovoltaic diode cell and (c) the current-voltage behavior due to shunt and series resistances.

over the voltage scan range, the maximum power point (MPP) is determined. An ideality factor, or fill factor (FF), is calculated by finding the ratio between the product of voltage

and current at the MPP and the product of voltage and current at ideal conditions (i.e. open circuit and short circuit). Using these measurements, we can also compare the output power of the device to the input power of a given light source to determine the PCE.

JV measurements are performed by varying an applied voltage, step-wise, from short circuit conditions to open-circuit conditions or vice versa. The forward and reverse scans, respectively, have a given scan rate which is determined by the change in voltage divided by the interval time between each measurement point (scan rate = dV/dt). The scan rate is an important parameter during measurement because it determines the current response coming from the cell. The current response is linked to the capacitive behavior of the cell and provides information suggesting how charges may be accumulating under different conditions (i.e. dark vs. light).

A solar cell typically shows a diode-like behavior and can generally be described by the equivalent circuit as shown in the bottom left-hand schematic of figure 5 (b). The PSC is represented by the photodiode. The resistor in series represents the deviation from ideal behavior at the Voc or the 'turn-on' voltage, and the parallel resistor (shunt resistance – R_{shunt}) describes deviation from ideal saturation current behavior due to leakage current effects. This change in behavior is shown in the bottom right-hand image of figure 5 (c). Here the dotted blue line is the ideal behavior, the red line shows actual behavior of a photovoltaic under illumination, and the dotted black lines are the slopes described by series and shunt resistances. It is important to note that perovskite solar cells do not always behave according to the ideal diode shown above.

This information can provide a good idea of overall electrical performance, but it does not provide evidence of specific mechanisms of recombination. Thus, it is often

necessary to pair it with other opto-electrical characterization methods such as ultraviolet-visible absorption spectroscopy (UV-vis), photoluminescence spectroscopy (PL), impedance spectroscopy (IS), and other time-dependent optical and electrical characterization techniques

2.3.1 Impact of Hysteresis on Current-Voltage Analysis

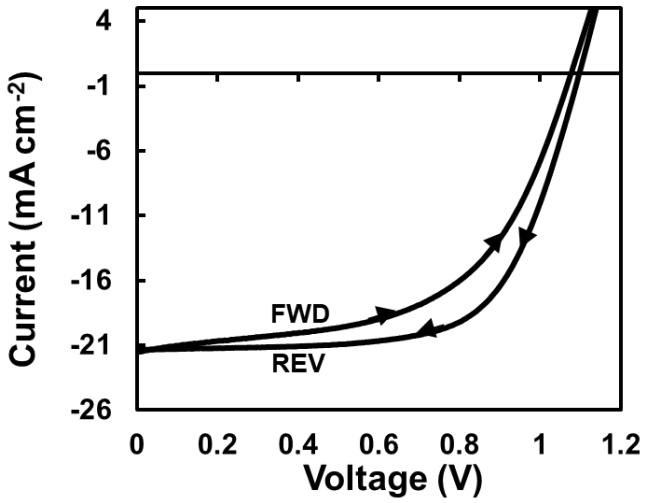

Figure 6 - Example of hysteresis between forward and reverse scans during JV measurements for PSCs.

A common phenomenon during JV characterization of PSCs is hysteresis between forward and reverse scans. This is caused by several intrinsic and extrinsic factors and is very difficult to control. Thus, it has become a topic of heavy study. Some extrinsic factors include scan rate, scan direction, voltage window, and pre-conditioning. These are all measurement-based parameters that can influence the JV response of the device. This information can indicate many different possible mechanisms such as an imbalance of charge extraction. Intrinsic factors include recombination at interfaces, charge trapping, and ion migration [27]. Debate over the the dominant origins of hysteresis is still on-going,

but it is generally considered to be due to an imbalance in the built in electric field generated during illumination. When charges accumulate at the interfaces, for example, they can screen the built-in field which dimishes charge transport into the ETL and/or HTL. While hysteresis is an important aspect in PSCs, it will not be a main point of discussion.

CHAPTER 3. PEROVSKITE SOLAR CELLS

3.1 Organic-Inorganic Perovskite Solar Cells

Since the discovery of methylammonium lead iodide as the sensitizer in dye-sensitized solar cells, organic-inorganic perovskite materials have been the center of focus in perovskite solar cell research. The organic-inorganic hybrids are branded as such due to the use of a small-molecule organic cation in the A site of the perovskite structure. Methylammonium (CH_3CH_2NH) This sets it apart from all other photovoltaic materials. A significant amount of studies were done to understand the role of the organic cation on the electronic properties, such as the band gap and ferroelectricity, and also the structural properties, such as rotational effects and bonding to BX_6 octahedral framework [28].

I began by fabricating $MAPbI_3$ solar cells by mostly following the conventional methods found in the literature. Once success was achieved in fabrication. Similar methods were employed to fabricate $Cs_{0.05}(MA_{0.17}FA_{0.83})_{0.95}Pb(I_{0.83}Br_{0.17})_3$ solar cells. This was the first step in understanding fabrication approaches for different compositions of perovskite materials.

3.1.1 Fabrication methods of $MAPbI_3$ solar cells

Transparent conductive oxide glass acts as the substrate for depositing each layer in the solar cell stack with fluorine-dope tin oxide (FTO) and indium-doped tin oxide (ITO) being the most common. FTO/glass (Sigma Aldrich) with a sheet resistance of ~15Ω/□ was Zn-etched and cleaned by sonicating in acetone, isopropyl alcohol, and ethanol, respectively, for 30 min each. The cleaned substrates were treated for 15 min in a UV-O_3 plasma cleaner.

Electron transport layer. A 0.15 M solution of titanium diisopropoxide bis(acetylacetonate) in n-butanol (filtered twice through 40µm filter) was spin-coated onto the FTO/glass substrates at 2000rpm for 30sec and then annealed at 500^{o}C for 30 min. Next, samples were submerged in a 40 mM $TiCl_4$ (aqueous) solution at 70^{o}C for 30min to 1hr. This forms the compact-TiO_2 layer (cp-TiO_2). Samples were cleaned with DI H_2O and ethanol. Another 15min treatment in UV-O_3 plasma was performed, and a 1:6 titania paste: methanol (anhydrous) solution was spin-cast onto the cp-TiO_2 layer. The next layer was annealed at 500^{o}C for 30 min to form the mesoporous TiO_2 layer (mp-TiO_2).

Perovskite layer. Equimolar amounts of MAI (created in house following methods in the literature) and PbI_2 were dissolved in a mixture of N,N-dimethylformamide (DMF)/ N,N-dimethylsulfoxide (DMSO) and stirred on a hotplate at 70^{o}C for several hours. The perovskite precursor was spin-coated onto UV-O_3 treated mp-TiO_2 substrates at 4000rpm for 30sec. After 7sec into the spin-coating process 0.6mL of diethyl ether was dropped onto the spinning substrate. The resulting films were annealed on a hotplate at 100^{o}C for 10 min. Note, perovskite deposition and annealing were performed in a N_2 atmosphere glovebox.

Hole transport layer. 72mg Spiro-MeOTAD was dissolved in 1 mL of chlorobenzene along with 17.5mL Li- bis(trifluoromethanesulfonyl)imide (TFSI) solution and 28.8µL 4-*tert*-butyl (TBP). The solution was spin-cast onto the perovskite films at 3000rpm for 30sec. The films were allowed to dry for several minutes and transferred to a thermal evaporation where 120nm of Ag was deposited as an electrode contact.

Each of the steps in the fabrication of the full perovskite solar cell stack of thin films is critical and requires careful attention to detail. The crystallization process of the

perovskite light-absorbing layer is one of the most important steps. The perovskite layer must convert into the proper phase to obtain good absorption and electrical properties. One way to quickly identify if the perovskite deposition was done correctly is if films appear dark-brown and have a mirror-like finish. This signifies a smooth morphology and high crystallinity.

Different methods for fabricating the perovskite layer have been developed including spin-coating, screen-printing, aerosol spray coating, and gas-phase deposition [29]. Spin-coating is the most common method employed. In this category are two methods: one-step [30] and two-step [31]. In the two-step method, a layer of PbI_2 dissolved in DMF is deposited. Then, MAI is deposited onto the PbI_2 film and annealed to crystalize the films. Early studies found this method had issues with crystallization because it was difficult to control the phase transformation of the film and the evaporation of the solvent. The one-step method was developed as a way to help control the crystallization rate via a solvent engineering [30].

The procedures for fabricating $MAPbI_3$ films via the one-step deposition method are described above and the spin-coating steps are shown in figure 7. The DMSO, which acts as a Lewis base, is added to a one-pot precursor ink solution to form an adduct with PbI_2 and MAI precursors, which act as Lewis acids [32]. The lone pair electrons on the end of the double-bonded oxygen atom in DMSO render it as an effective electron donor for PbI_2 which originally want to gain more iodide anions. The formation of this Lewis acid-base adduct slows down the crystallization process. During spin-coating, diethyl ether is dropped which is immiscible with the perovskite precursors but miscible with DMF. DMF is washed away by the non-polar solvent, while $MAI{\cdot}PbI_2{\cdot}DMSO$ remains. After spin-

coating a transparent intermediate phase is formed [33]. Annealing on the hotplate removes DMSO and initiates transition and crystallization of $MAPbI_3$. This method was shown to result in better films with fewer pinholes than those with only DMF as the solvent [34].

3.1.2 Results and Discussion

Several parameters are important to keep track of. The precursor solution ratio is important and small variations in molar ratio can impact film quality. Additionally, the time of anti-solvent applications has a large effect on the film morphology. For example, smooth perovskite films were only able to be fabricated when dropping diethyl ether ~7sec after beginning the spin-coating of the perovskite precursor. Figure 7 shows the morphology of the perovskite films made within the appropriate window and films outside the window (before and after). The further away from the 7 second "drop time" resulted in more turbid films. During spin-coating, excess solvent is removed until supersaturation occurs and $MAPbI_3$ nuclei begin to form. If the anti-solvent is dropped to early, it removes the excess solvent and does not allow the formation of an intermediate phase, whereas, dropping too late allows $MAPbI_3$ nuclei to start crystallization, thus forming a non-homogeneous film [35].

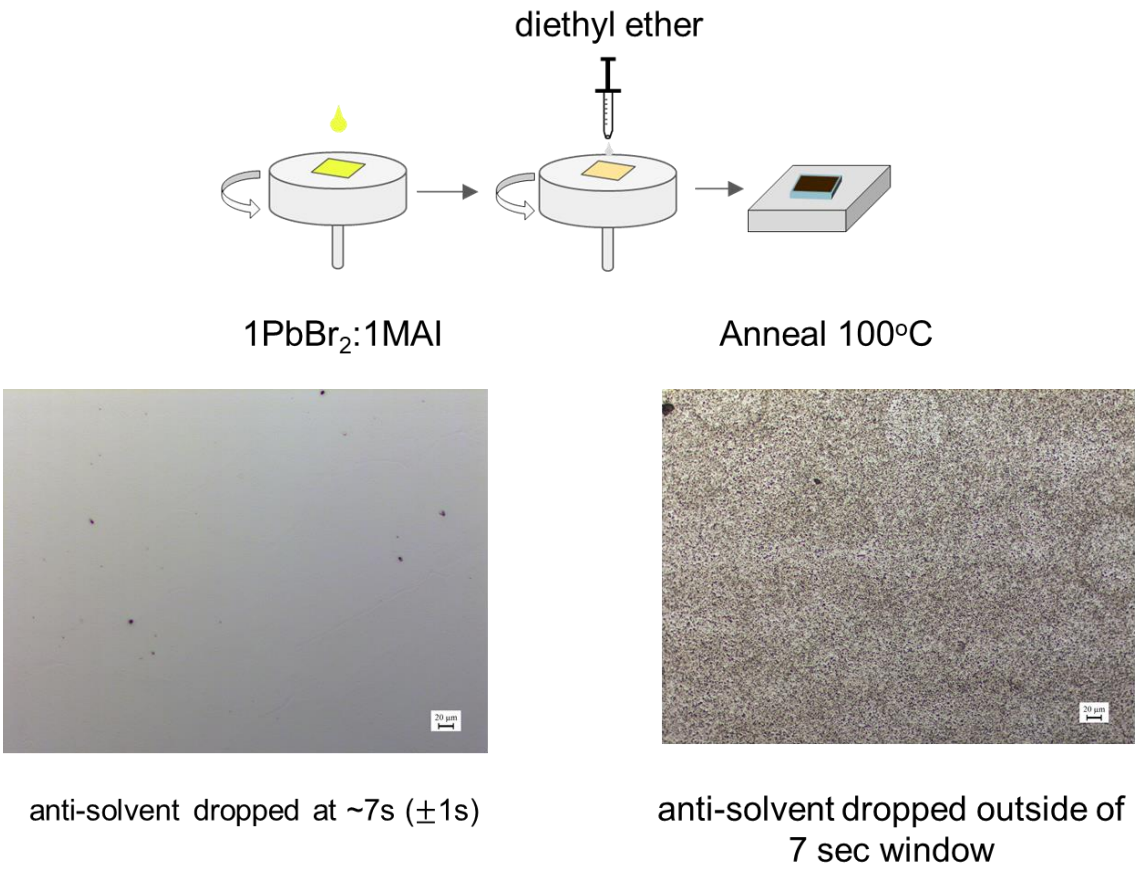

Figure 7 - Optical microscope images $MAPbI_3$ films after spin coating with different diethyl ether drop times.

The morphology of the perovskite film and quality of each layer is especially sensitive to processing protocols and effects of human error. Some studies have tried fabricating completely pinhole-free films by using techniques such as co-evaporation or adding surfactants to the precursor solution [36]. Spin-coating is a process that can easily result in non-uniformities and pinholes due to surface defects and particles in the precursor solution. Thus, it is very important to properly clean and treat each surface as well as, make sure the precursor solutions are well-dissolved and filtered (if necessary).

Optical microscope images and scanning electron microscope images show the effect of pinholes on the morphology of the TiO_2 and perovskite films (Figure 8). The large size and shape of the pinhole suggests is likely due to a surface contaminant. Pinholes that occur in the bottom layer can carry effects to subsequent layers after and eventually cause shorts such as shown in the JV curve in figure

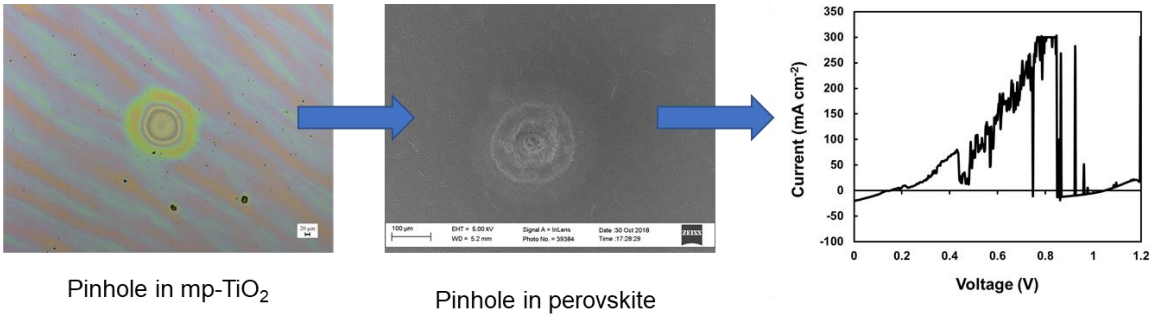

Figure 8 - (left) Optical microscope image of pinhole in mp-TiO_2 (scale bar = 20µm). (middle) SEM image of pinhole in $MAPbI_3$ film (scale bar = 100µm). (right) JV curve of solar cells with large pinholes visible to the naked eye.

After working on controlling negative impacts such as pinholes and poor film morphology, high-quality $MAPbI_3$ solar cells were achieved. Figure 9 (a) shows the UV-vis spectra of the typical $MAPbI_3$ perovskite film, and figure 9 (b) is the estimated band gap determined from the Tauc Plot corresponding to the UV-vis spectra. Figure 9 (c) shows the dark-brown/black color and mirror-like quality of the $MAPbI_3$ film. The reverse scan of the champion cell is shown in the figure 9 (d).

Mixed-cation and mixed-halide perovskite solar cells with the composition $Cs_{0.05}(MA_{0.17}FA_{0.83})_{0.95}Pb(I_{0.83}Br_{0.17})_3$ were fabricated following similar methods to the $MAPbI_3$ solar cells. Following a one-step deposition method, precursor materials were dissolved in a 4:1 (v:v) solution of DMF/DMSO in the following molar ratio (1 FAI: 1.1 PbI_2 : 0.2 MABr: 0.2

$PbBr_2$). CsI was dissolved in DMSO to make a 1.5M solution and the appropriate amount was added to achieve ~5% Cs in the composition. Only a small amount is necessary to offer stabilization to the lattice and reduce the change of $FAPbI_3$ regions to the non-photoactive hexagonal phase [13].

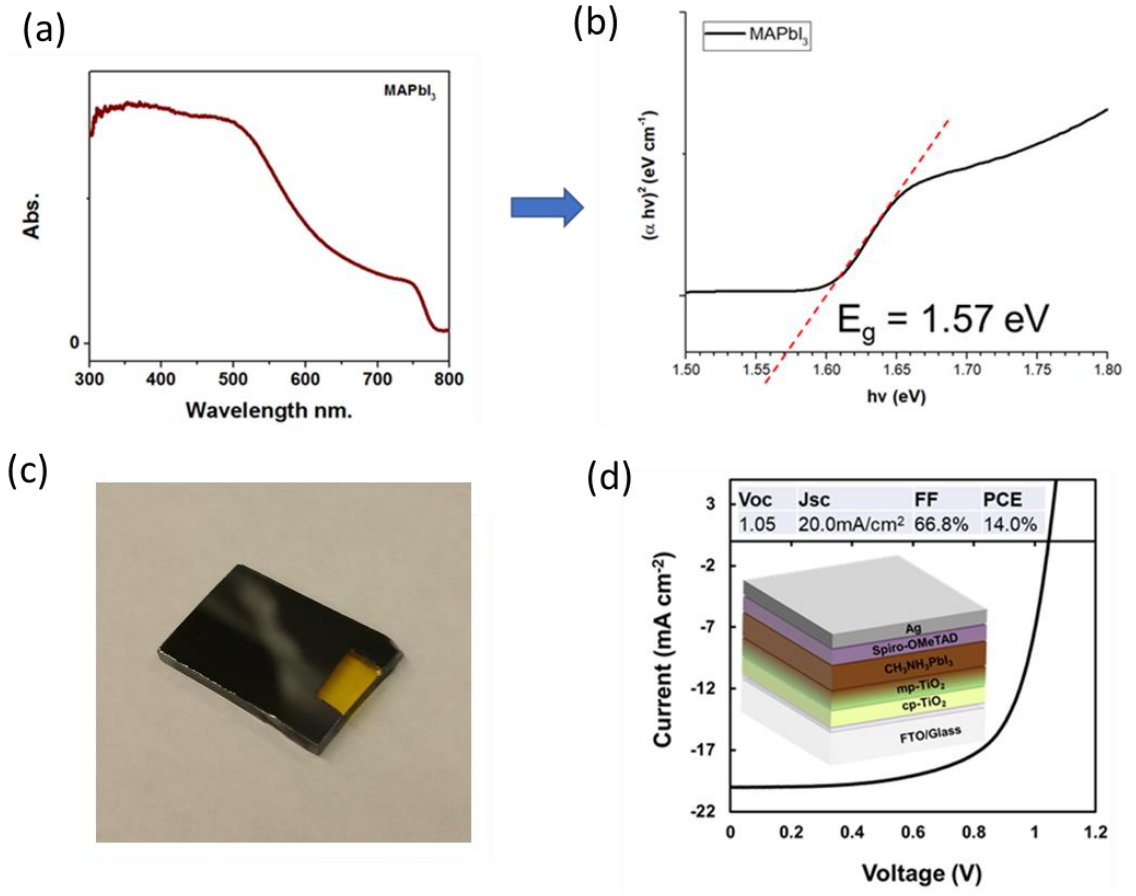

Figure 9 - (a) UV-vis of $MAPbI_3$ film. (b) Tauc plot with estimated band gap of $MAPbI_3$ film determined from UV-vis. (c) Camera image of $MAPbI_3$ film. (d) Reverse scan of a $MAPbI_3$ solar cell.

Further engineering of processing protocols were necessary to find the proper anti-solvent drop time and precisely control the precursor ratio amounts. The results showed similar films with improved photovoltaic properties as shown in figure 10. The most notable improvement from the $MAPbI_3$ results is the increase in FF to over 70%. This

indicates a large reduction in charge carrier recombination and suggests a reduction in trap sites within the perovskite and likely at the interfaces as well. A consistent increase in PCE was observed for most cells with an increase of almost 4% for the reported champion cells.

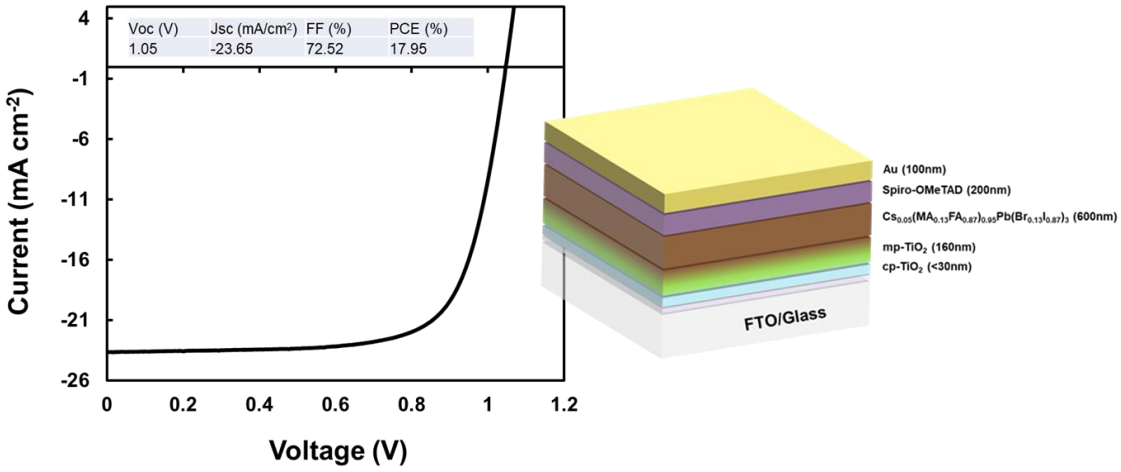

Figure 10 - Reverse JV scan of champion $Cs_{0.05}(MA_{0.17}FA_{0.83})_{0.95}Pb(I_{0.83}Br_{0.17})_3$ solar cell and schematic of stack with approximate layer thickness determined from cross-sectional SEM.

A cross-sectional SEM image was taken of several $Cs_{0.05}(MA_{0.17}FA_{0.83})_{0.95}Pb(I_{0.83}Br_{0.17})_3$ solar cells with the best image shown in the top of figure 11. From this image the thickness of the devices was estimated and were found to be within reasonable accuracy to the literature [13]. Similarly, an SEM image of the perovskite morphology after spin-coating onto mp-TiO_2 shows similar grain size to studies using similar one-step deposition method (figure 11 – bottom).

The results of organic-inorganic perovskite solar cells with different compositions show the first step towards developing methods and techniques for fabricating perovskite solar cells with different compositions.

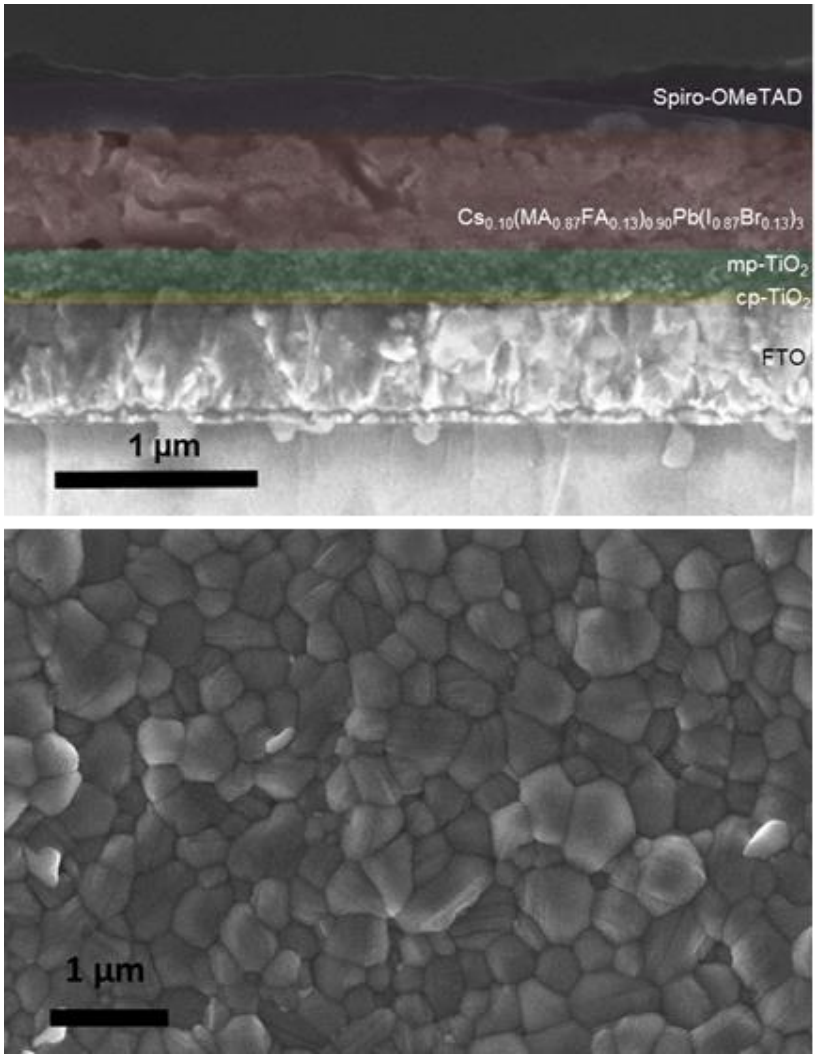

Figure 11 - (top) Cross-sectional SEM of $Cs_{0.05}(MA_{0.17}FA_{0.83})_{0.95}Pb(I_{0.83}Br_{0.17})_3$ solar cell. (bottom) SEM image of $Cs_{0.05}(MA_{0.17}FA_{0.83})_{0.95}Pb(I_{0.83}Br_{0.17})_3$ surface.

3.2 All-inorganic Perovskite Solar Cells

The typical organic-inorganic perovskite absorber enables high-efficiency solar cells, over 20%, which is competitive with commercial silicon solar cells, but these materials still lack stability. Currently, the most stable organic-inorganic perovskite solar cells last for approximately one year [37]. Although they are less efficient, all-inorganic

perovskite materials such as $CsPbBr_3$ have become of increasing interest due to superior stability to oxygen, moisture, and heat. The improved stability is attributed to the inorganic Cesium cation which replaces hygroscopic MA and FA cations. The organic cations easily absorb moisture and cause decomposition [37].

3.2.1 Fabrication of $CsPbBr_3$ solar cells

All-inorganic $CsPbBr_3$ films are more difficult to prepare than their organic-inorganic counterparts. This is due to the poor solubility of CsBr and $PbBr_2$ in at high concentration [38]. Thus, anti-solvent approaches are not viable.

One common process found in the literature, and the process used in this study, is a two-step, spin-coating process [38]. To fabricate $CsPbBr_3$ bulk films, I used a modified version of the two-step spin-coating deposition process (Figure 12). FTO/glass substrates were cleaned by sonicating in acetone, IPA, and EtOH, respectively, and then treated via oxygen plasma. Compact TiO_2 films and mesoporous TiO_2 layers were deposited using the same procedures described previously (see page XX). The TiO_2 covered substrates were pre-heated at 90^{o}C and a 1M solution of $PbBr_2$ (Sigma Aldrich, 99.999%) in DMF was spin-coated at 2000 rpm for 30 sec. The $PbBr_2$ films were then dried on a hotplate at 70^{o}C in ambient atmosphere for 30 minutes. CsBr/MeOH (15mg/mL) was spin-coated onto the $PbBr_2$ at the same speed and then annealed at 250^{o}C on a hotplate. This process was repeated up to four times to improve the stoichiometric ratio and achieve $CsPbBr_3$.

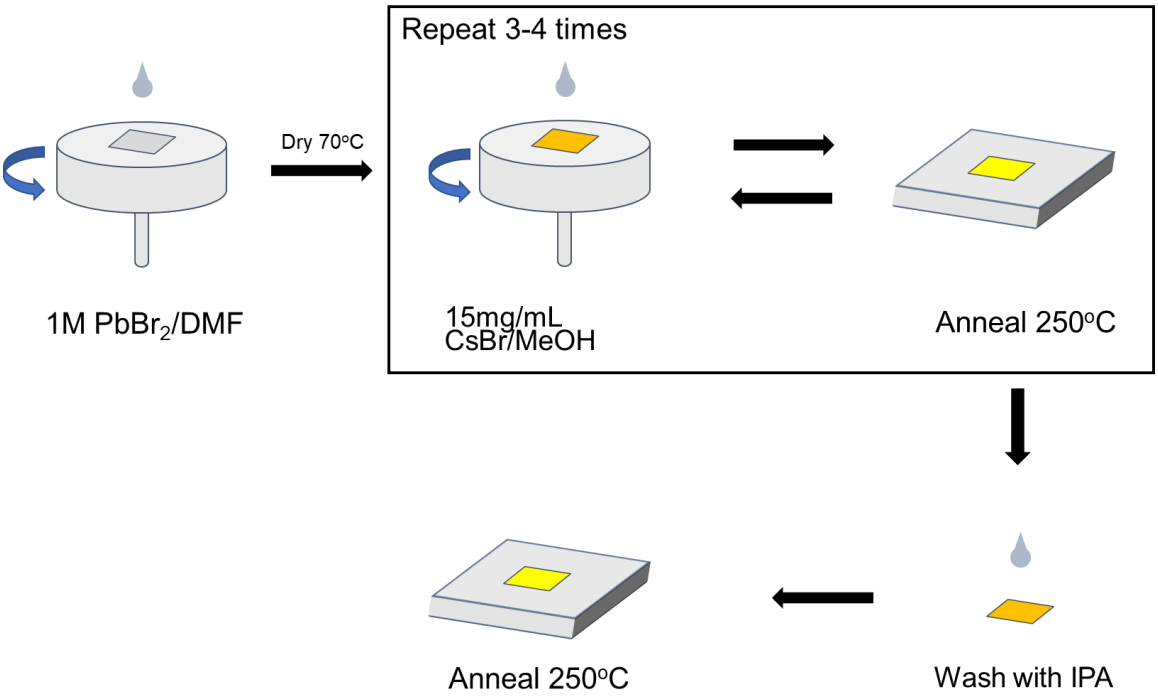

Figure 12 - Schematic of two-step spin-coating procedure for fabricating $CsPbBr_3$ thin films.

The conversion to $CsPbBr_3$ was confirmed via UV-vis absorption spectroscopy and is shown in figure 13. The onset of a peak at 520nm and the presence of a peak at 375nm is indicative of the formation of cubic $CsPbBr_3$ phase, as compared to the blue-shifted onset of the $PbBr_2$ peak. The difference in color between white $PbBr_2$ films and yellow $CsPbBr_3$ films is another indicator as evident in the right-hand images in figure 13. Another important note to make is the appearance of a large peak around 315nm in the UV-vis spectrum of $CsPbBr_3$. This peak is attributed to the presence of a 0D perovskite material, Cs_4PbBr_6, in contrast to the 3D structure of $CsPbBr_3$ [39]. The low dimensionality comes from a general formula, A_nBX_{2+n}, where n=1 for 3D perovskite structure. As the amount of CsBr to $PbBr_2$ increases, 'n' also increases), and the dimensionality of the perovskite is lowered due to the additional Cs cations which push the $PbBr_6$ octahedral apart. The

$CsPbBr_3$ crystal structure consists of corner sharing $PbBr_6$ octahedra, but the octahedra of the Cs_4PbBr_6 composition are isolated (no longer corner sharing) which further increases quantum confinement of charge carriers and increases the exciton binding energy, thus increasing the photoluminescence properties [39]. While this is beneficial for applications in light-emitting diodes, the increase in exciton decay and emission of photons reduces the PCE for solar cell applications. For this reason, I explored how the processing parameters affected the presence of the Cs_4PbBr_6 peak at 315nm in the UV-vis spectrum.

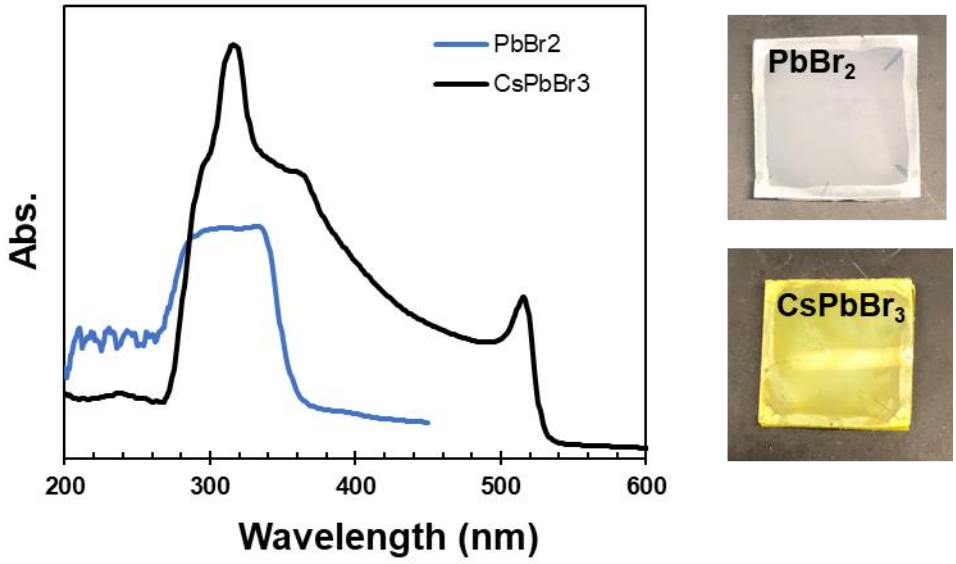

Figure 13 - UV-vis spectra of $PbBr_2$ film (blue) and $CsPbBr_3$ film (black), and camera images of each of the subsequent films.

3.2.2 Results and Discussion

It is difficult to control the conversion process of $PbBr_2$ to $CsPbBr_3$. Since, CsBr is not added in the proper stoichiometric ratio to the precursor solution, several deposition cycles of CsBr/MeOH, and subsequent annealing steps, are required to initiate the crystallization of cubic $CsPbBr_3$. The original steps for annealing after the deposition of

CsBr/MeOH solution required up to 5min annealing at 250^{o}C. Yet, during the first spin-coating step, films turned from a yellow color back to white. The top right-hand graph in figure 14 shows the effect of annealing time after the first deposition of CsBr/MeOH. Reducing the annealing time to 30 sec resulted in conversion to $CsPbBr_3$ while increased annealing time up to 2 min resulted in a conversion almost completely back to $PbBr_2$ with the presence of a new peak (likely from Cs_4PbBr_6).

Conversion from $PbBr_2$ was achieved via annealing for 30sec after 1 spin-coating step of CsBr/MeOH, but the absorption of the film was very low compared to the films that went through 3-4 depositions of CsBr/MeOH. Thus, multiple spin-coating steps with subsequent annealing for 30sec after each step was performed (Figure 14 – top left). UV-vis spectra show that a second spin-coating step of CsBr/MeOH after annealing for 30sec improved the absorption. Yet, the appearance of the Cs_4PbBr_6 peak still became evident. Further repetitions of spin-coating and annealing for 30sec showed further increase of the Cs_4PbBr_6 peak. This finding shows that processing time needs to be controlled to improve the CsBr:$PbBr_2$ ratio when fabricating films using this approach. Optical images of films under a black-light are shown in bottom of figure 14. These images coincide with the UV-vis spectra in the left-hand graph of figure 14. Here, we see that as the peak at ~315nm increases, the luminescence of the films increase. This may be attributed to presence of Cs_4PbBr_6 and confinement of $CsPbBr_3$ phase [40].

Further study needs to be done using techniques such as x-ray diffraction and x-ray photoelectron spectroscopy to reveal the presence and relative amounts of each phase, as well, as the spatial distribution.

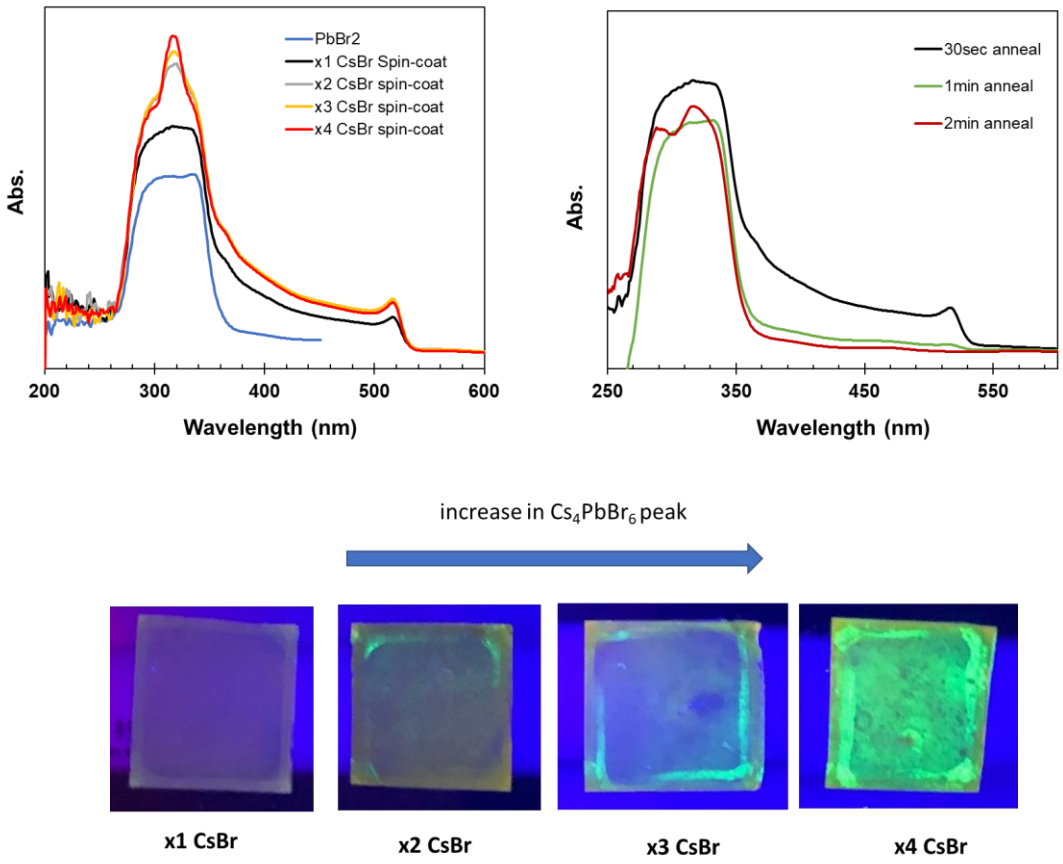

Figure 14 - (left) UV-vis of films after different number of CsBr/MeOH deposition cycles. (right) Comparison of UV-vis spectra for different annealing times, at 250ºC, after one deposition cycle of CsBr/MeOH. (bottom) Camera images of luminescent films under black-light. The films correspond to the number of CsBr/MeOH spin-coating steps (in the right-hand UV-vis spectra).

Engineering of the processing parameters and controlling the annealing time of each CsBr/MeOH step resulted in $CsPbBr_3$ films with improved photovoltaic properties. The ETL (cp-TiO_2 and mp-TiO_2) and HTL (Spiro-MeOTAD) in the all-inorganic devices are the same as used in the organic-inorganic devices described in chapter 2, and the same procedures were followed to fabricate these layers. The first successful attempts at fabricating all-inorganic perovskite solar cells resulted in low PCE (3.8%) and low FF (<50%), but high V_{OC} (1.3V) was obtained indicating good quality of contact layers.

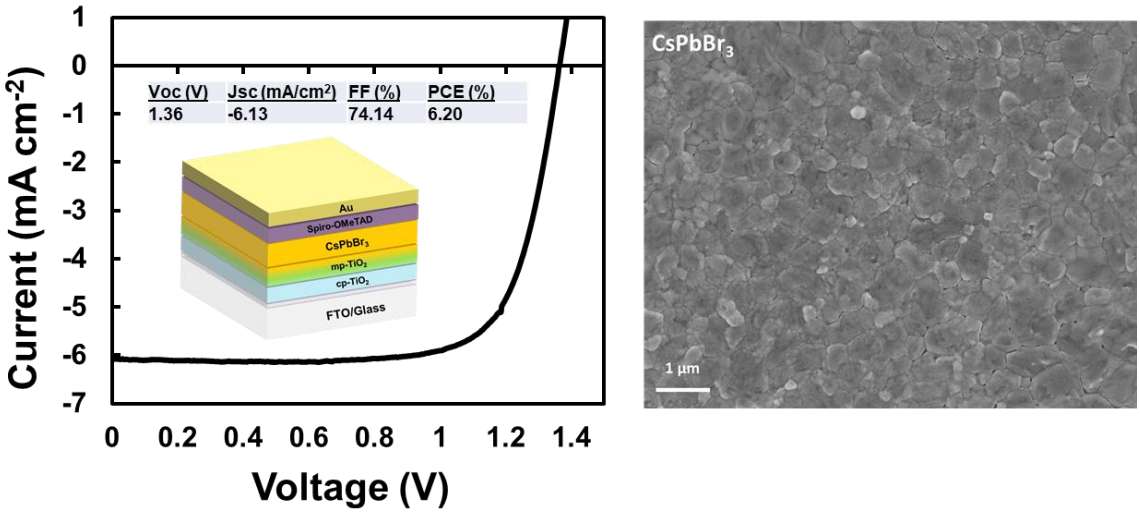

Figure 15 - $CsPbBr_3$ champion cell using 3 CsBr/MeOH deposition cycles with reduced annealing time. (right) SEM image of $CsPbBr_3$ morphology.

The best solar cell was fabricated using 3 deposition cycles of CsBr/MeOH and controlling the annealing time to be between 30 seconds and 1 min for each cycle (figure 15). The final annealing time after IPA washing was kept at 5 min. The FF was drastically improved to over 70%. The PCE was also improved by a few percentage points up to a max of 6.2%, and the V_{OC} was also improved to upwards of 1.36V. The J_{SC} stayed approximately the same between the early batches and later batches of solar cells. Improving the conductivity (and Jsc) of $CsPbBr_3$ films should be the next focus. This may be achieved by improving the grain size which reduces recombination within the perovskite. The SEM image in the right-hand of figure 15 shows the $CsPbBr_3$ morphology. A mixture of small grains and larger grains is present. Additionally, some of the larger grains appear to be separated by gaps which may be the cause of reduced charge transport and low J_{SC}. Further improvement of processing by controlling annealing time and reducing the Cs_4PbBr_6 peak, but maintaining good absorption in the longer wavelength

region is expected to further improve performance, but this is a good first step towards fabricating high-quality $CsPbBr_3$ solar cells.

In conclusion, all-inorganic perovskite solar cells, of the composition $CsPbBr_3$, were fabricated using a two-step spin-coating process. The ratio of 3D to lower dimensionality perovskite formed during fabrication was found to be affected by annealing procedures. This, in turn, affects the resulting light absorption and photovoltaic properties of the PSCs. By controlling the annealing time between subsequent CsBr/MeOH deposition cycles, the amount of the Cs_4PbBr_6 was able to be tuned. This study shows the first steps towards fabricating high-quality $CsPbBr_3$ solar cells by through crystal phase tuning. Future efforts should focus on interface modification, improving grain boundaries, and tuning composition (e.g. adding iodide) to improve overall PCE.

CHAPTER 4. PEROVSKITE SOLAR CELLS FOR USE IN LOW-EARTH ORBIT

The International Space Station (ISS) is equipped with an out-board materials science laboratory called the Materials International Space Station Experiment (MISSE). This allows materials and devices for aerospace applications to be tested under multiple conditions simultaneously such as ultra-high vacuum, (10^{-6} to 10^{-9} torr), large temperature variation, high concentration of atomic oxygen, and high energy radiation (UV and cosmic rays, etc.). The ISS is in low-Earth orbit (LEO) which is ~400km above the planet and orbits approximately 15.5 times a day (or every 92 minutes).

Only a few studies so far have researched the potential applications of PSCs for use in space. Cardinaletti et al. sent both organic (polymer) solar cells and organic-inorganic $MAPbI_3$ solar cells into the stratosphere via a large balloon designed to withstand the upper atmosphere conditions [41]. This study was part of the Optical Sensors based on CARbon materials (OSCAR) mission which sent the solar cells to a height of 32 km above the Earth for ~5hr flight. The typical photovoltaic parameters were tracked *in situ* at max point power along with temperature during flight. $MAPbI_3$ devices showed a decrease in FF during the initial float phase due to the temperature decrease to ~220K. This is a commonly observed phenomenon for organic semiconductors and may also be due to increased interfacial recombination at the ETL [42]. The performance improved at the end of the float phase (peak altitude) as temperature increased showing the reversible nature of temperature effects.

In this chapter, I will outline the results of engineering perovskite solar cells to be sent to the ISS on MISSE-10, which is scheduled to fly December 2019. Two types of perovskite absorber layer (organic-inorganic versus inorganic) and two types of HTLs (Spiro-MeOTAD versus poly(3-hexylthiophene-2,5-diyl) (P3HT)) will be compared. Three slight variations of PSC were fabricated as follows:

(1) All-inorganic $CsPbBr_3$ perovskite solar cells (labeled AI in results)

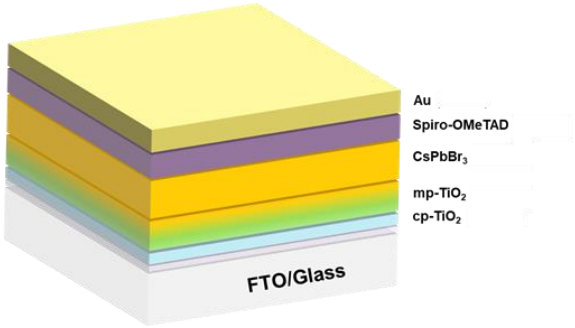

(2) Organic-inorganic $Cs_{0.05}(MA_{0.17}FA_{0.83})_{0.95}Pb(I_{0.83}Br_{0.17})_3$ perovskite solar cells with Spiro-MeOTAD as the HTL. (labeled OI-Spiro in results)

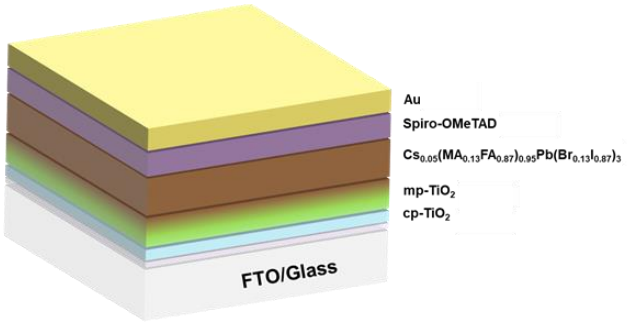

(3) Organic-inorganic $Cs_{0.05}(MA_{0.17}FA_{0.83})_{0.95}Pb(I_{0.83}Br_{0.17})_3$ perovskite solar cells with P3HT as the HTL. (labeled OI-P3HT in results)

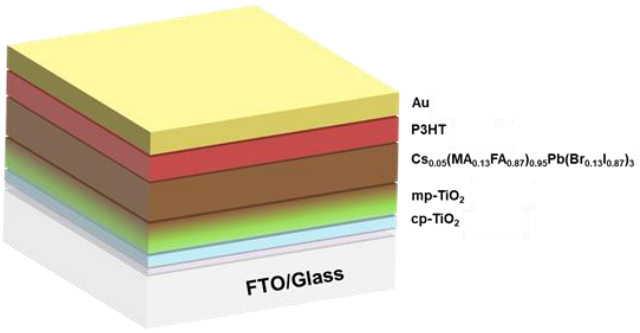

The stability of PSCs is hard to maintain even on Earth, so the goal of this study was to fabricate all-inorganic ($CsPbBr_3$) PSCs to test the stability against organic-inorganic perovskite solar cells ($Cs_{0.05}(MA_{0.17}FA_{0.83})_{0.95}Pb(I_{0.83}Br_{0.17})_3$). Additionally, the time period between delivering the samples and installment onto the ISS is ~6 months. Thus, it is expected that $CsPbBr_3$ solar cells will better maintain their properties during the storage time before launch. The reason these compositions were chosen is because $CsPbBr_3$ can be stable to temperatures up to 250^{o}C and above.

4.1 Perovskite Solar Cell Package Engineering

Most of the work herein consists of developing a way to attach perovskite solar cells to the package which will be loaded onto the MISSE console. The total device consists of a metal holder (package) with pins that are used for making electrical connection to the solar cell via gold wires. A PSC attached to the package and cover glass to seal the entire device. The main challenge was attaching the PSCs to the package. PSCs are fabricated by depositing each layer on FTO/glass substrates and gold is deposited as the final layer which contains both top and bottom electrodes on the same side of the sample (Figure 17). Since light is transmitted through the glass side of the substrate to be absorbed by the perovskite, the samples needed to be flipped upside down. Figure 16 shows the package, cover glass,

and a PSC. The perovskite solar cell fits onto the package and top and bottom electrodes are attached to the gold pins. The cover glass is then placed on top of the package and sealed. To make sure electrical contact could be made to the pins, a 'platform' was developed by thermally evaporating a robust metal conducting layer onto a masked glass slide. Note that each PSC device contains three separate cell 'pads' (Figure 17 - left). A platform was made by thermally evaporating a metal conductive pathway from each top electrode and the bottom electrode. The right-hand image in figure 17 shows a cartoon schematic of how the platform traces are connected to the pins via gold wires. The numbers (1, 2, and 3) in figure 17 are corresponding to each solar cell pad. Two connections are made from the bottom electrode for redundancy (these are labeled as ground).

An initial test was done by thermally evaporating 200nm of silver onto a masked-off glass substrate. The glass was thoroughly cleaned in acetone, IPA, and ethanol and treated with UV-O_3. A PSC was attached using a small amount of Ag paste and annealed on a hotplate at 100^{o}C for 30 min. The JV characteristics of the PSC were tested using a solar simulator (AM1.5) before and after it was attached to the Ag platform. Results from the JV analysis are shown in figure 19, and only a small decay in the $J_{SC,}$ FF, and PCE was observed. While the thermally evaporated silver provided a good enough electrical contact, it had poor adhesion to the glass substrate. Thus, ~100nm of chromium was thermally evaporated as an adhesion layer and ~200nm of gold was deposited (instead of silver) as the electrically conducting layer.

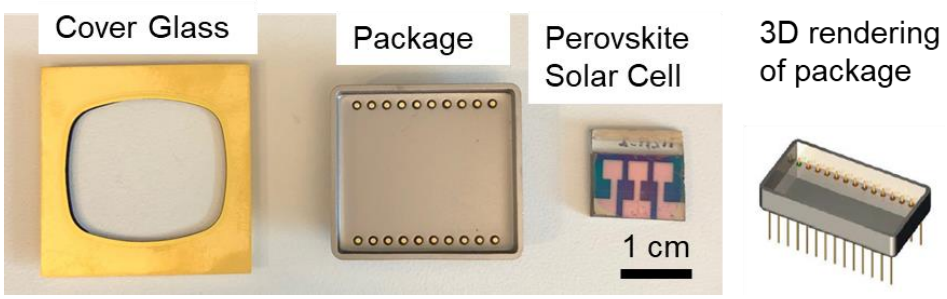

Figure 16 - Camera images of the cover glass and package, a perovskite solar cell, and a 3D rendering of the package from a different angle to see pins for electrical connection.

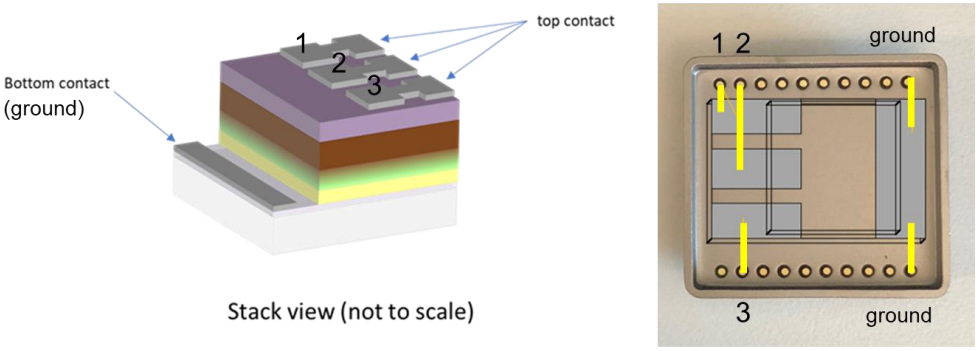

Figure 17 - (left) The stack view of a perovskite solar cell which shows top and bottom contacts are on the top side of the solar cell. (right) Schematic representation of PSC on platform with gold wires (yellow lines) making electrical connection to package pins. Note: top contacts for each solar cell 'pad' are labeled 1, 2, and 3. The bottom contact is labeled as ground.

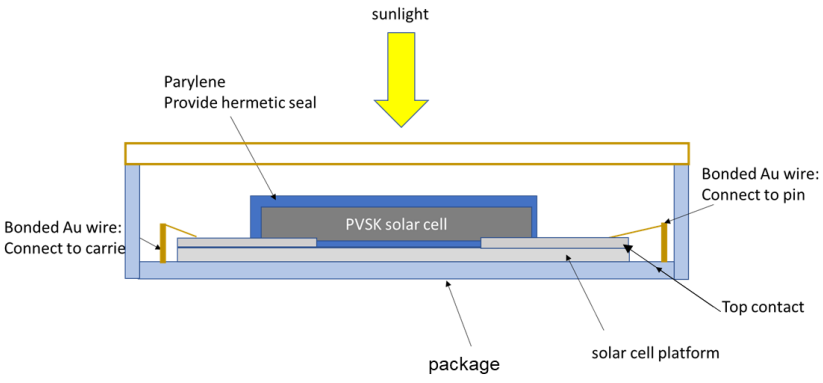

Figure 18 - Side view schematic of a PSC attached to package and encapsulated.

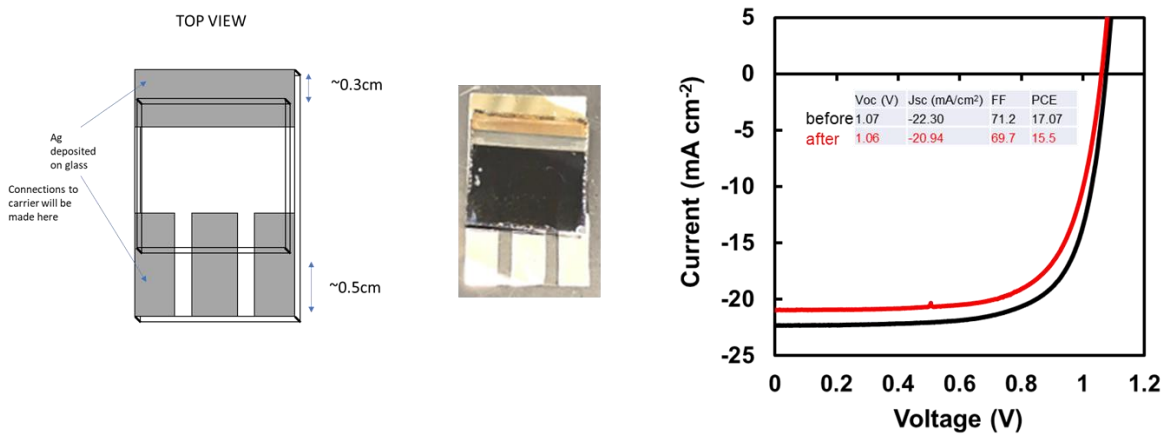

Figure 19 - (left) Schematic of solar cell platform. (middle) Camera image of PSC on Ag-coated glass slide platform. (right) JV curves before and after attaching solar cell to platform.

4.2 Encapsulation

The cover glass is expected to provide some degree of encapsulation for the solar cells, as well as, some protection against UV radiation. Even so, there was still some concern that the solar cells may degrade during transfer and further testing before launch. Thus, encapsulation of devices was performed after the solar cells were attached and wire-bonded to the package.

Parylene is the name for a class of chemical vapor deposited (CVD) poly(p-xylylene) polymers that are commonly used in the micro-electronics industry to protect circuit boards [43]. The CVD process enables formation of highly uniform pinhole free films which creates an excellent barrier to moisture and provides low gas permeability. Moisture protection is key for helping to protect organic-inorganic PSCs. Additionally, it has high UV and thermal stability, as well as, low coefficient of thermal expansion (CTE). High CTE mismatch between the encapsulant and device can cause the tears or breaks to occur

which expose the device. The cover glass will provide an extra barrier in the case of parylene degrading or breaking.

The deposition process goes through three main steps: sublimation, pyrolysis, and deposition. During sublimation a dimer of raw material is heated to 150^{o}C under high vacuum which vaporizes the material. The temperature increases to 690^{o}C which cleaves the dimer bonds and turns the material into highly-energetic monomers. The monomer gas is released into the ambient temperature chamber containing the samples to be coated, and the monomer parylene deposits onto every surface to reduce the energy of the monomer. During deposition the monomers bond together making a highly compact, uniform, thin polymer film.

A 5μm layer of parylene-C (chlorine functionalized) was deposited via CVD onto a PSC device before being attached to the package to test the effect of the polymer layer on the photovoltaic properties, and no significant change was observed (figure 20). after the solar cells were attached to the platforms and wire-bonded to the packages. Several connections were made to connect the PSC devices to the platform and the package, so a parylene coating should help protect the soldered joints from corrosion and provide some mechanical stability.

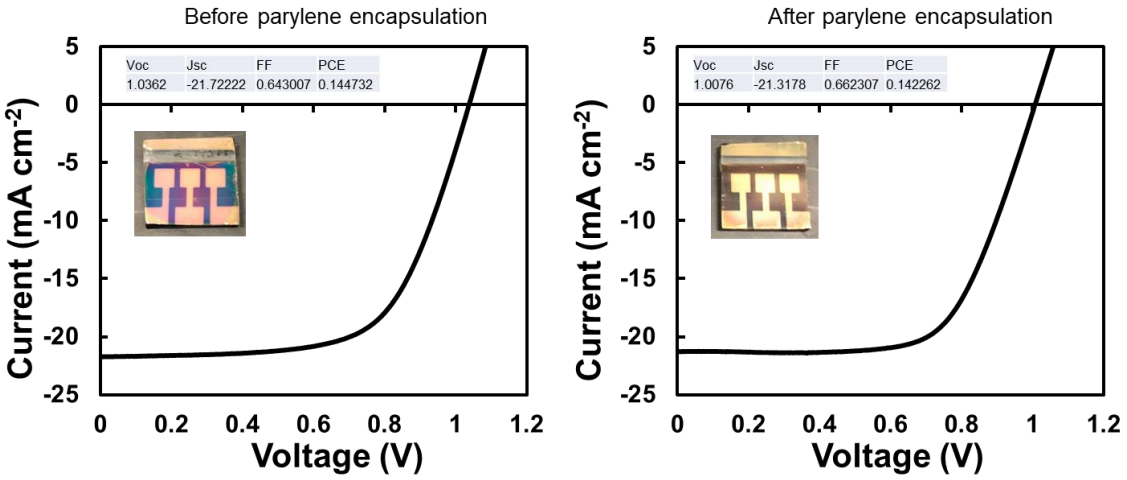

Figure 20 - JV characteristics of a $Cs_{0.05}(MA_{0.17}FA_{0.83})_{0.95}Pb(I_{0.83}Br_{0.17})_3$ solar cell before parylene encapsulation (left) and after parylene encapsulation (right).

4.3 Results

Current-voltage analysis was performed on all the fabricated cells. Ten cells in total were fabricated. Five of the samples were AI, four samples were OI-Spiro, and one sample was OI-P3HT (note: see page 25 for reference to labeling of devices). The AI solar cells were the best performing cells in terms of FF and survivability of the packaging process. All of the OI-Spiro and OI-P3HT saw degradation in all JV parameters during the packaging process. This is most likely due to over exposure to ambient atmosphere during attachment of the solar cells to the platform and package, and exposure to air during annealing during wire-bonding. It is important to perform as many steps as possible in inert atmosphere, or reduce ambient air exposure of organic-inorganic perovskite materials. On the other hand, three of the five AI-PSCs maintained most of their JV characteristics. Remarkably, one of the AI samples even resulted in improved performance after being attached to the package.

The AI champion cell resulted in a PCE of 5.71%, a V_{OC} of 1.28V, a J_{SC} of -6.16mA/cm^2, and FF of 72.2% (Figure 13 XX) during reverse scan. Additionally, this champion cell remained stable during several months of storage and even saw a rise in efficiency during this time. Forward JV scan of the device showed diminished performance and is characteristic hysteresis of performance. Table XX compares the JV parameters for each pad on the champion AI solar cell. The average of all forward and reverse scans of each pad shows an average PCE of 4.43% and an average FF of 64.6%.

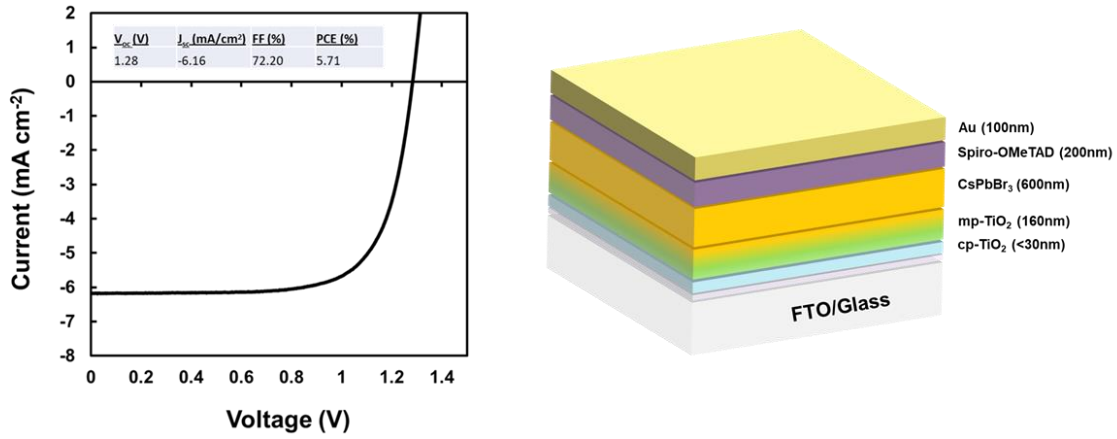

Figure 21 - JV curve of champion all-inorganic solar cell after being attached to package, encapsulated with parylene, and enclosed by cover glass.

Table 1 - JV characteristics of champion AI ($CsPbBr_3$) solar cell after being attached to package and after encapsulation. Pad # corresponds to Fig. 17. (*fwd* denotes forward scan and *rev* denotes reverse scan)

Pad #	V_{oc} (V)	J_{SC} (mA/cm^2)	FF (%)	PCE (%)
1-fwd	1.34	-4.43	60.45	3.59
2-fwd	1.30	-5.40	58.72	4.13
3-fwd	1.24	-5.02	48.74	3.05
1-rev	1.36	-4.60	75.91	5.13
2-rev	1.30	-5.34	71.43	4.96
3-rev	1.28	-6.16	72.20	5.71
Average	1.30	-5.22	64.57	4.43
St. Dev.	0.04	-0.53	9.45	0.92

The champion OI-Spiro solar cell, after attaching to the package, resulted in a PCE of 12%, a FF of 50%, a Jsc of 22.4mA/cm^2, and a Voc of 1.05V. This result shows that although Jsc and Voc retained high values, typical to OI-Spiro solar cells, performance degraded significantly due to an increase in series resistance and shunt resistance, evidenced by the reduced FF. Further characterization is necessary to determine the exact

cause of this phenomenon. The best reverse scan of the OI-P3HT sample resulted in a Voc of 0.82V, a Jsc of -11.44mA/cm^2, a FF of 44%, and a PCE of 4.17%.

Three different types of PSCs were fabricated to test functionality and stability in LEO conditions. All-inorganic, $CsPbBr_3$, and organic-inorganic $Cs_{0.05}(MA_{0.17}FA_{0.83})_{0.95}Pb(I_{0.83}Br_{0.17})_3$ solar cells were fabricated following methods described in chapters 2 and 3. Additionally, a $Cs_{0.05}(MA_{0.17}FA_{0.83})_{0.95}Pb(I_{0.83}Br_{0.17})_3$ solar cell was fabricated with P3HT as the HTL instead of the conventional Spiro-MeOTAD to see the effect of two different polymer HTLs. Significant engineering was done to properly attach the solar cells to packages that will allow JV data to be collected *in situ* during orbit on the ISS as part of the MISSE-10 mission. Initial measurements showed that several of the organic-inorganic solar cells underwent significant degradation during the packaging process, while a few of the all-inorganic solar cells were able to retain good performance. The champion cell used an all-inorganic perovskite photo-absorbing layer, and shows the most promise for use in LEO due to the better thermal and overall environmental stability of the $CsPbBr_3$ perovskite composition.

CHAPTER 5. CONCLUSIONS AND FUTURE OUTLOOKS

In this study, I presented the fabrication and photovoltaic characteristic results of organic-inorganic $MAPbI_3$ and $Cs_{0.05}(MA_{0.17}FA_{0.83})_{0.95}Pb(I_{0.83}Br_{0.17})_3$, as well as, a study on the processing effects on the formation of $CsPbBr_3$ films for all-inorganic perovskite solar cells. The goal of the study was to develop perovskite solar cells that could be stable in low-Earth orbit. Some common issues that occur during fabrication were presented and discussed including the effects of pinholes in various device layers such as TiO_2 and the perovskite layer, and the importance of finding the appropriate anti-solvent dripping time.

The photovoltaic properties of the organic-inorganic solar cells were improved from a PCE of 14% for $MAPbI_3$ to a PCE of nearly 18% for $Cs_{0.05}(MA_{0.17}FA_{0.83})_{0.95}Pb(I_{0.83}Br_{0.17})_3$. This initial result shows the importance of compositional engineering to improve the light-harvesting capability and electronic properties of the perovskite material.

All-inorganic $CsPbBr_3$ solar cells were fabricated and studied as alternatives due to higher thermal stability to their organic-inorganic counterparts. A two-step spin-coating process was used, but did not result in full conversion of $PbBr_2$ to $CsPbBr_3$. The ratio of 3D to lower dimensionality perovskite formed during fabrication was found to be affected by annealing procedures. This, in turn, affects the resulting light absorption and photovoltaic properties of the PSCs. By controlling the annealing time between subsequent CsBr/MeOH deposition cycles, the amount of the Cs_4PbBr_6 was able to be tuned. A champion $CsPbBr_3$ solar cell was achieved with a FF of 74% which is the highest of any of the other types of devices.

Lastly, PSCs were fabricated to send for testing in LEO conditions. Engineering approaches, design conditions, and preliminary photovoltaic data is discussed. A-inorganic, $CsPbBr_3$, and organic-inorganic $Cs_{0.05}(MA_{0.17}FA_{0.83})_{0.95}Pb(I_{0.83}Br_{0.17})_3$ solar cells were fabricated following methods described in chapters 2 and 3. Significant engineering was done to properly attach the solar cells to packages that will allow JV data to be collected *in situ* during orbit on the ISS as part of the MISSE-10 mission. Organic-inorganic solar cells underwent significant degradation during the packaging process. This is likely due to exposure to ambient conditions during packaging and possibly high annealing temperatures during the wire-bonding process. Care should be taken in the future to do all processes under inert atmospheres. The champion cell was an all-inorganic, $CsPbBr_3$ perovskite photo-absorbing layer. Compact and mesoporous TiO_2 were used as the ETL and Spiro-OMeTAD was used as the HTL with thermally deposited Au as the contact. The best reverse scan showed high Voc of 1.36V and high FF of 75% with a PCE of 5.2%. This device shows the most promise to survive LEO conditions given the better thermal and overall environmental stability of the $CsPbBr_3$ perovskite composition.

The future of perovskite solar cell technology appears to be bright as efficiency continues to increase and new types of perovskite materials and compositions are developed with enhanced stability. For the future of this work, replacement of the organic HTL, Spiro-OMeTAD, is a key step to further improving long-term stability at higher temperatures. Initial study using a carbon electrode as a HTL-free $CsPbBr_3$ achieved an efficiency of only ~2%. Further improvements of the carbon electrode should result in a highly stable perovskite solar cell that may find future use in aerospace applications.

REFERENCES

1. Kojima, A., et al., *Organometal Halide Perovskites as Visible-Light Sensitizers for Photovoltaic Cells.* Journal of the American Chemical Society, 2009. **131**(17): p. 6050-6051.

2. Lee, M.M., et al., *Efficient Hybrid Solar Cells Based on Meso-Superstructured Organometal Halide Perovskites.* Science, 2012. **338**(6107): p. 643.

3. Yang, W.S., et al., *Iodide management in formamidinium-lead-halide–based perovskite layers for efficient solar cells.* Science, 2017. **356**(6345): p. 1376.

4. Galkowski, K., et al., *Determination of the exciton binding energy and effective masses for methylammonium and formamidinium lead tri-halide perovskite semiconductors.* Energy & Environmental Science, 2016. **9**(3): p. 962-970.

5. Tsai, H., et al., *High-efficiency two-dimensional Ruddlesden–Popper perovskite solar cells.* Nature, 2016. **536**: p. 312.

6. Zhu, Z., et al., *Highly Efficient and Stable Perovskite Solar Cells Enabled by All-Crosslinked Charge-Transporting Layers.* Joule, 2018. **2**(1): p. 168-183.

7. Iles, P.A., *Future of photovoltaics for space applications.* Progress in Photovoltaics: Research and Applications, 2000. **8**(1): p. 39-51.

8. Kurtz, S., et al., *A comparison of theoretical efficiencies of multi-junction concentrator solar cells.* Progress in Photovoltaics: Research and Applications, 2008. **16**(6): p. 537-546.

9. Kaltenbrunner, M., et al., *Flexible high power-per-weight perovskite solar cells with chromium oxide–metal contacts for improved stability in air.* Nature Materials, 2015. **14**: p. 1032.

10. Hörantner, M.T., et al., *The Potential of Multijunction Perovskite Solar Cells.* ACS Energy Letters, 2017. **2**(10): p. 2506-2513.

11. Stoumpos, C.C., C.D. Malliakas, and M.G. Kanatzidis, *Semiconducting Tin and Lead Iodide Perovskites with Organic Cations: Phase Transitions, High Mobilities, and Near-Infrared Photoluminescent Properties.* Inorganic Chemistry, 2013. **52**(15): p. 9019-9038.

12. Jeon, N.J., et al., *Compositional engineering of perovskite materials for high-performance solar cells.* Nature, 2015. **517**: p. 476.

13. Saliba, M., et al., *Cesium-containing triple cation perovskite solar cells: improved stability, reproducibility and high efficiency.* Energy & Environmental Science, 2016. **9**(6): p. 1989-1997.

14. Akbulatov, A.F., et al., *Probing the Intrinsic Thermal and Photochemical Stability of Hybrid and Inorganic Lead Halide Perovskites.* The Journal of Physical Chemistry Letters, 2017. **8**(6): p. 1211-1218.

15. Wang, K., et al., *All-inorganic cesium lead iodide perovskite solar cells with stabilized efficiency beyond 15%*. Nature Communications, 2018. **9**(1): p. 4544.

16. Liang, J., et al., *All-Inorganic Perovskite Solar Cells.* Journal of the American Chemical Society, 2016. **138**(49): p. 15829-15832.

17. Yuan, H., et al., *All-inorganic CsPbBr3 perovskite solar cell with 10.26% efficiency by spectra engineering.* Journal of Materials Chemistry A, 2018. **6**(47): p. 24324-24329.

18. Miyata, A., et al., *Direct measurement of the exciton binding energy and effective masses for charge carriers in organic–inorganic tri-halide perovskites.* Nature Physics, 2015. **11**: p. 582.

19. Meloni, S., et al., *Valence and conduction band tuning in halide perovskites for solar cell applications.* Journal of Materials Chemistry A, 2016. **4**(41): p. 15997-16002.

20. Peña, M.A. and J.L.G. Fierro, *Chemical Structures and Performance of Perovskite Oxides.* Chemical Reviews, 2001. **101**(7): p. 1981-2018.

21. Saparov, B. and D.B. Mitzi, *Organic–Inorganic Perovskites: Structural Versatility for Functional Materials Design.* Chemical Reviews, 2016. **116**(7): p. 4558-4596.

22. Milot, R.L., et al., *Temperature-Dependent Charge-Carrier Dynamics in CH3NH3PbI3 Perovskite Thin Films.* Advanced Functional Materials, 2015. **25**(39): p. 6218-6227.

23. Ahmad, W., et al., *Inorganic CsPbI3 Perovskite-Based Solar Cells: A Choice for a Tandem Device.* Solar RRL, 2017. **1**(7): p. 1700048.

24. Grancini, G., et al., *One-Year stable perovskite solar cells by 2D/3D interface engineering.* Nature Communications, 2017. **8**: p. 15684.

25. Zhang, W., et al., *Recent Advance in Solution-Processed Organic Interlayers for High-Performance Planar Perovskite Solar Cells.* Advanced Science, 2018. **5**(7): p. 1800159.

26. Zhou, H., et al., *Interface engineering of highly efficient perovskite solar cells.* Science, 2014. **345**(6196): p. 542.

27. Azpiroz, J.M., et al., *Defect migration in methylammonium lead iodide and its role in perovskite solar cell operation.* Energy & Environmental Science, 2015. **8**(7): p. 2118-2127.

28. Senocrate, A., I. Moudrakovski, and J. Maier, *Short-range ion dynamics in methylammonium lead iodide by multinuclear solid state NMR and 127I NQR.* Physical Chemistry Chemical Physics, 2018. **20**(30): p. 20043-20055.

29. Ansari, M.I.H., A. Qurashi, and M.K. Nazeeruddin, *Frontiers, opportunities, and challenges in perovskite solar cells: A critical review.* Journal of Photochemistry and Photobiology C: Photochemistry Reviews, 2018. **35**: p. 1-24.

30. Jeon, N.J., et al., *Solvent engineering for high-performance inorganic–organic hybrid perovskite solar cells.* Nature Materials, 2014. **13**: p. 897.

31. Lee, J.-W. and N.-G. Park, *Two-step deposition method for high-efficiency perovskite solar cells.* MRS Bulletin, 2015. **40**(8): p. 654-659.

32. Lee, J.-W., H.-S. Kim, and N.-G. Park, *Lewis Acid–Base Adduct Approach for High Efficiency Perovskite Solar Cells.* Accounts of Chemical Research, 2016. **49**(2): p. 311-319.

33. Li, Y., et al., *Anti-solvent dependent device performance in CH3NH3PbI3 solar cells: the role of intermediate phase content in the as-prepared thin films.* Sustainable Energy & Fuels, 2017. **1**(5): p. 1041-1048.

34. Ahn, N., et al., *Highly Reproducible Perovskite Solar Cells with Average Efficiency of 18.3% and Best Efficiency of 19.7% Fabricated via Lewis Base Adduct of Lead(II) Iodide.* Journal of the American Chemical Society, 2015. **137**(27): p. 8696-8699.

35. Zhang, H., et al., *Understanding the Effect of Delay Time of Solvent Washing on the Performances of Perovskite Solar Cells.* ACS Omega, 2017. **2**(11): p. 7666-7671.

36. Liu, M., M.B. Johnston, and H.J. Snaith, *Efficient planar heterojunction perovskite solar cells by vapour deposition.* Nature, 2013. **501**: p. 395.

37. Fu, Q., et al., *Recent Progress on the Long-Term Stability of Perovskite Solar Cells.* Advanced Science, 2018. **5**(5): p. 1700387.

38. Kulbak, M., D. Cahen, and G. Hodes, *How Important Is the Organic Part of Lead Halide Perovskite Photovoltaic Cells? Efficient CsPbBr3 Cells.* The Journal of Physical Chemistry Letters, 2015. **6**(13): p. 2452-2456.

39. Saidaminov, M.I., et al., *Pure Cs4PbBr6: Highly Luminescent Zero-Dimensional Perovskite Solids.* ACS Energy Letters, 2016. **1**(4): p. 840-845.

40. Ling, Y., et al., *Composite Perovskites of Cesium Lead Bromide for Optimized Photoluminescence.* The Journal of Physical Chemistry Letters, 2017. **8**(14): p. 3266-3271.

41. Cardinaletti, I., et al., *Organic and perovskite solar cells for space applications.* Solar Energy Materials and Solar Cells, 2018. **182**: p. 121-127.

42. Shao, S., et al., *Efficient Perovskite Solar Cells over a Broad Temperature Window: The Role of the Charge Carrier Extraction.* Advanced Energy Materials, 2017. **7**(22): p. 1701305.

43. Maier, G., *Polymers for microelectronics.* Materials Today, 2001. **4**(5): p. 22-33.